Available online at www.sciencedirect.com
SCIENCE DIRECT®
Journal of Magnetic Resonance 177 (2005) 329–335
JMR Journal of Magnetic Resonance
www.elsevier.com/locate/jmr

Communication

Improved time efficiency and accuracy in diffusion tensor microimaging with multiple-echo acquisition

Vikas Gulani [a,b,*], Thomas Weber [a], Thomas Neuberger [a], Andrew G. Webb [a,c]

[a] Experimentelle Physik 5, Physikalisches Institut, Universität Würzburg, Am Hubland, 97074 Würzburg, Germany
[b] Department of Radiology, University of Michigan, 1500 East Medical Center Drive, Ann Arbor, MI 48109-0030, USA
[c] Department of Bioengineering, 206 Hallowell Building, Penn State University, University Park, PA 16802, USA

Received 21 December 2004; revised 19 August 2005
Available online 23 September 2005

Abstract

In high-field NMR microscopy rapid single-shot imaging methods, for example, echo planar imaging, cannot be used for determination of the apparent diffusion tensor (ADT) due to large magnetic susceptibility effects. We propose a pulse sequence in which a diffusion-weighted spin-echo is followed by multiple gradient-echoes with additional diffusion weighting. These additional echoes can be used to calculate the ADT and T_2^* maps. We show here that this results in modest but consistent improvements in the accuracy of ADT determination within a given total data acquisition time. The method is tested on excised, chemically fixed rat spinal cords.

Keywords: Apparent diffusion tensor; Multiple-echo; Imaging sequence; Spinal cord

1. Introduction

Apparent diffusion tensor (ADT) mapping requires the acquisition of at least seven images with diffusion weighting in different directions [1,2]. However, accurate calculation of various anisotropy indices [3] and signal-to-noise (S/N) considerations often require a larger number of images to be acquired, a constraint that can result in long data acquisition times. In clinical/human applications, this potential problem of long experiments is in large part offset by application of rapid imaging techniques; in particular echo planar imaging (EPI). In very high-field magnetic resonance microscopy, however, EPI generally cannot be used due to large magnetic susceptibility effects. For this reason, and because microscopy experiments are often conducted on excised and fixed samples, rather long imaging times are typically encountered in ADT microscopy [4–10].

To reduce imaging time, several groups have taken advantage of the inherent cylindrical symmetry of many samples (such as white matter tracts and muscle fibers) to reduce the number of directions along which diffusion-weighted images must be obtained to characterize the tensor [5,11,12]. However, while such methods are extremely useful when applied to appropriate samples, they cannot be used in many cases where the sample geometry is not known, or when multiple fiber orientations are encountered within a voxel. Multiple-echo acquisition has been a well-studied method for reducing imaging time in MRI [13,14]. Reduced-encoding techniques, in which the high spatial frequency information from reference images are combined with images acquired with reduced k-space coverage, have also been shown to be an effective way to reduce the total data acquisition time [15]. Multiple spin-echoes have previously been applied to diffusion NMR to collect multiple spectra and calculate the ADC and T_2 [16] and to reduce the time required for diffusion tensor microimaging [5]. However, perhaps due to difficulties in implementation of this sequence stemming from creation of spurious echoes [13,14,17] and odd and even echo signal oscillations caused by imperfect 180° pulses [18], this route has not found widespread use in diffusion tensor microimaging. A fast spin-echo sequence has been proposed for in vivo microimaging

* Corresponding author.
E-mail address: vikas@umich.edu (V. Gulani).

1090-7807/$ - see front matter © 2005 Elsevier Inc. All rights reserved.
doi:10.1016/j.jmr.2005.08.007

[19] and was extended to enable bulk motion correction during post-processing [20]. This method has proven to be efficient for in vivo applications, though just as the sequence in reference [5], complications stemming from B_1 inhomogeneities and generation of spurious echoes must be considered in the analysis and application.

Here, we propose an alternative sequence which is much easier to implement than the spin-echo based methods, and consists of a diffusion-weighted spin-echo, followed by a train of gradient-echoes with additional diffusion weighting provided by bipolar gradient pulses (Fig. 1). All of the images are used to reconstruct an ADT and a T_2^* map. We demonstrate the feasibility of this method on excised, fixed rat spinal cords.

2. Methods

Experiments were conducted on cervical spinal cords excised from 12-week-old female Dark Agouti (DA) rats, and fixed with 4% paraformaldehyde. Post-fixation, the cords were immersed in phosphate-buffered saline (PBS—800 g H_2O, 0.4732 g H_2PO_4, and 0.4734 g Na_2HPO_4, pH 7.4) and placed in a 5 mm NMR tube. The procedure is in compliance with the Institutional Review Board (IRB) of the University Hospital of Regensburg, where the cords were excised. The imaging sequence in Fig. 1 was implemented on a Bruker 750 MHz spectrometer (Bruker Biospin, Ettlingen, Germany), equipped with imaging gradients (1 T/m maximum gradient strength), and a home-built 5 mm diameter Alderman–Grant resonator. The sample temperature was 20 °C.

Imaging parameters include TR 1.1 s, TE 13.7 ms (spin-echo), 23.1 ms (first gradient-echo) and 32.9 ms (second gradient-echo), 400 μm slice thickness, 5 mm × 5 mm FOV, 128 × 128 data matrix (39 μm in-plane resolution, 0.61 nL voxel volume), and 8 signal averages. For diffusion weighting, $\delta = 2$ ms and $\Delta = 6$ ms were used for the first echo (i.e., the spin-echo) and $\delta = \Delta = 2.2$ ms for all the following echoes. Maximal diffusion gradient strengths were 0.7 T/m. Seven and 13 gradient configurations were chosen for the spin-echo experiments, and additional diffusion weighting was provided along the same orientation for the gradient-echoes. The configurations of the diffusion gradients and also the calculated b-factors are summarized in Table 1. Image numbers 1–7 summarize the settings for the single-echo 7 image experiment, 1–13 for the single-echo 13 image experiment, and 1–39 for the 39 image experiments. The gradient configurations and the b-factors for the 21 image experiments are contained in image numbers 1–7, 14–20, and 27–33. As can be seen, the maximum calculated absolute b-value was approximately 1380 s/mm^2 for the first echo images, with additional maximal diffusion weighting of approximately 310 s/mm^2 for each of the subsequent echoes.

The data were processed using Matlab (The Mathworks, Natick, MA, USA). The diffusion and T_2^* signal decay was modeled as follows:

$$I = I_0 \exp\left(-\sum_{i,j,k} b_{ij,k} D_{ij} - (TE - TE_1)/T_2^*\right), \tag{1}$$

$$b_{ij,k} = \gamma^2 \int \left(\int_0^{t_k} G_i \, \mathrm{d}t' \int_0^{t_k} G_j \, \mathrm{d}t'\right) \mathrm{d}t, \tag{2}$$

where k represents the echo number, and i and j the various diffusion gradient directions. For each image, the b-matrix was calculated by numerically integrating the gradient shapes used according to Eq. (2). Substituting this b-matrix and echo time (relative to the echo time, TE_1, of the spin-echo) for each image into Eq. (1) is followed by a least squares fit for D_{ij}, the six independent components of the apparent diffusion tensor. Two rotational invariants were obtained. The trace (Tr) and fractional anisotropy (FA) were calculated from the eigenvalues (λ_i) of the ADT according to Eqs. (3) and (4) given below.

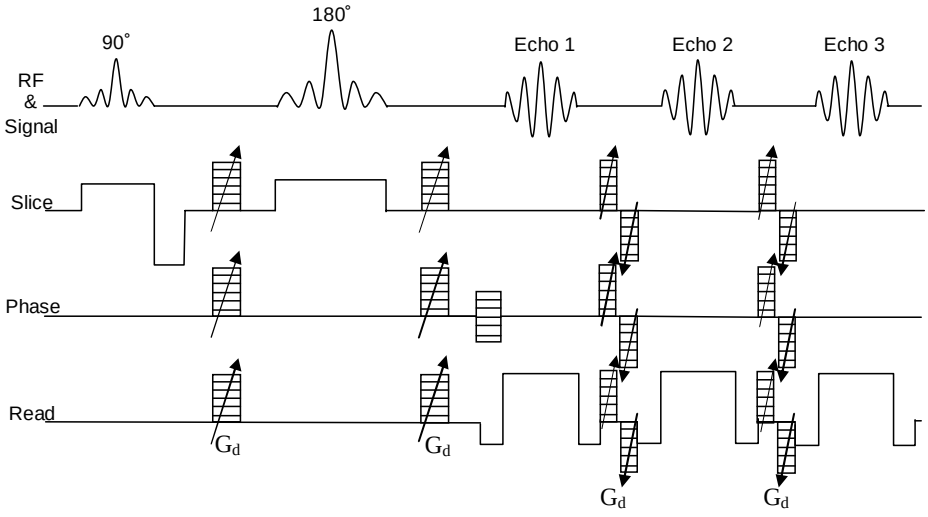

Fig. 1. Imaging sequence employing a spin-echo followed by two gradient-echoes to improve diffusion tensor microimaging efficiency. G_d represents the diffusion encoding gradients.

Table 1
The gradient configurations and calculated b-matrix for each image

Image number	Gradient configuration (g_{xx}, g_{yy}, g_{zz})	b_{xx} (s/mm^2)	b_{xy} (s/mm^2)	b_{xz} (s/mm^2)	b_{yy} (s/mm^2)	b_{yz} (s/mm^2)	b_{zz} (s/mm^2)
1	(0,0,0)	0	0	0	0	0	61
2	(1,0,0)	1080	0	143	0	0	61
3	(0,1,0)	0	0	0	1080	143	61
4	(0,0,1)	0	0	0	0	0	1380
5	$(\sqrt{2}/2, \sqrt{2}/2, 0)$	540	540	101	540	101	61
6	$(\sqrt{2}/2, 0, \sqrt{2}/2)$	540	0	641	0	0	802
7	$(0, \sqrt{2}/2, \sqrt{2}/2)$	0	0	0	540	641	802
8	$(\sqrt{2}/2, -\sqrt{2}/2, 0)$	540	−540	101	540	−101	61
9	$(\sqrt{2}/2, 0, -\sqrt{2}/2)$	540	0	−439	0	0	399
10	$(0, -\sqrt{2}/2, \sqrt{2}/2)$	0	0	0	540	−641	802
11	$(\sqrt{3}/3, \sqrt{3}/3, -\sqrt{3}/3)$	360	360	−278	360	−278	256
12	$(-\sqrt{3}/3, \sqrt{3}/3, \sqrt{3}/3)$	360	−360	−442	360	442	585
13	$(\sqrt{3}/3, -\sqrt{3}/3, \sqrt{3}/3)$	360	−360	442	360	−442	585
14	(0,0,0)	0	0	0	0	0	61
15	(1,0,0)	1388	0	143	0	0	61
16	(0,1,0)	0	0	0	1388	143	61
17	(0,0,1)	0	0	0	0	0	1687
18	$(\sqrt{2}/2, \sqrt{2}/2, 0)$	694	694	101	694	101	61
19	$(\sqrt{2}/2, 0, \sqrt{2}/2)$	694	0	795	0	0	956
20	$(0, \sqrt{2}/2, \sqrt{2}/2)$	0	0	0	694	795	956
21	$(\sqrt{2}/2, -\sqrt{2}/2, 0)$	694	−694	101	694	−101	61
22	$(\sqrt{2}/2, 0, -\sqrt{2}/2)$	694	0	−593	0	0	553
23	$(0, -\sqrt{2}/2, \sqrt{2}/2)$	0	0	0	694	−795	956
24	$(\sqrt{3}/3, \sqrt{3}/3, -\sqrt{3}/3)$	463	463	−380	463	−380	358
25	$(-\sqrt{3}/3, \sqrt{3}/3, \sqrt{3}/3)$	463	−463	−545	463	545	688
26	$(\sqrt{3}/3, -\sqrt{3}/3, \sqrt{3}/3)$	463	−463	545	463	−545	688
27	(0,0,0)	0	0	0	0	0	61
28	(1,0,0)	1695	0	143	0	0	61
29	(0,1,0)	0	0	0	1695	143	61
30	(0,0,1)	0	0	0	0	0	1995
31	$(\sqrt{2}/2, \sqrt{2}/2, 0)$	848	848	101	848	101	61
32	$(\sqrt{2}/2, 0, \sqrt{2}/2)$	848	0	949	0	0	1110
33	$(0, \sqrt{2}/2, \sqrt{2}/2)$	0	0	0	848	949	1110
34	$(\sqrt{2}/2, -\sqrt{2}/2, 0)$	848	−848	101	848	−101	61
35	$(\sqrt{2}/2, 0, -\sqrt{2}/2)$	848	0	−747	0	0	707
36	$(0, -\sqrt{2}/2, \sqrt{2}/2)$	0	0	0	848	−949	1110
37	$(\sqrt{3}/3, \sqrt{3}/3, -\sqrt{3}/3)$	565	565	−483	565	−483	461
38	$(-\sqrt{3}/3, \sqrt{3}/3, \sqrt{3}/3)$	565	−565	−648	565	648	790
39	$(\sqrt{3}/3, -\sqrt{3}/3, \sqrt{3}/3)$	565	−565	648	565	−648	790

The configuration for image numbers 1–7 were used for the single-echo, 7 image experiments; 1–13 for the single-echo, 13 image experiments; 1–7, 14–20, and 27–33, for the multiple-echo, 21 image experiments, and 1–39 for the multiple-echo, 39 image experiments.

$$\mathrm{Tr} = \lambda_1 + \lambda_2 + \lambda_3, \tag{3}$$

$$\mathrm{FA} = \sqrt{\frac{3}{2}\frac{\sum_i (\lambda_i - \bar{\lambda})^2}{\sum_i \lambda_i^2}}. \tag{4}$$

The above analysis was first performed for the spin-echo signals only, using either 7 or 13 diffusion-encoding directions. Comparison was then made to results obtained by incorporating the signals from the additional two gradient-echoes, corresponding to either 21 (7×3) or 39 (13×3) images. T_2^* maps were also obtained for the multiple-echo data sets. Imaging times were 2.2 h to obtain 7/21 images, and 4.1 h for 13/39 images.

For each data set, regions of interest (ROIs) in the cord were selected, and the Tr/3 and FA for these regions compared for the data from the simple spin-echo and the new sequence. Uncertainties were estimated by calculating the standard deviation within the ROIs. For gray matter (GM) an ROI was drawn in the central GM, and for white matter (WM) in the dorsal or ventral WM. ROIs were chosen anatomically and sizes range from 48 (central gray matter) to 78 pixels (lateral column white matter).

A data set with higher spatial resolution was also acquired with 13/39 images, TR 1.1 s, TE values 15.9, 28.4, and 40.9 ms, respectively, FOV 6×6 mm, 256×256 matrix (23 μm in-plane resolution with a slice thickness of 600 μm and 0.32 nL voxel volume), $\delta = 2$ ms and $\Delta = 6$ ms for the first echo and $\delta = \Delta = 2.2$ ms for the following echoes. Total data acquisition time was 8.1 h. This high resolution data set was acquired using a linear birdcage resonator (Bruker Biospin, Ettlingen, Germany).

3. Results

Fig. 2 depicts FA maps obtained from (A) 7 images, (B) 13 images, (C) 21 images, and (D) 39 images, respectively.

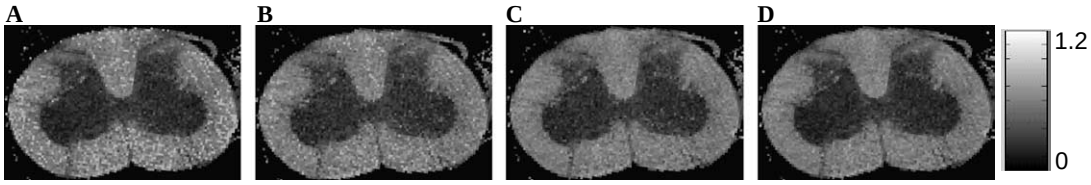

Fig. 2. FA maps constructed from (A) 7 spin-echo images, (B) 13 spin-echo images, (C) 21 images (7 spin-echo and 14 gradient-echo) from the new sequence, and (D) 39 images (13 spin-echo and 26 gradient-echo) from the new sequence. Resolution is 39 μm × 39 μm × 400 μm, voxel volume 0.61 nL.

FA values from gray and white matter regions in the cord are shown in Table 2 and Tr values are summarized in Table 3. Calibration experiments were also performed using pure water: in these cases smaller b-values were used due to water's larger diffusion coefficient, and the results are also shown in Tables 2 and 3. Table 4 summarizes FA values for the ventral cord region of the cord for three different spinal cords. The FA maps from the high resolution data sets are shown in Fig. 3, reconstructed from (A) 13 images and (B) 39 images. Finally, a sample T_2^* map from a 39 image experiment is illustrated in Fig. 4. As a reference for future work, the obtained S/N in the $b = 0$ spin-echo image from the high resolution data set was 28 and 47 for the dorsal columns white matter and central gray matter, respectively.

4. Discussion

As can be seen from Fig. 2, particularly in the white matter regions, the FA maps reconstructed from 7 and 13 spin-echo images are noisier than those obtained from 21 and 39 images from the combined spin- and gradient-echoes. This is also illustrated by the smaller error bars for the FA and Tr values in Tables 2 and 3 for the multiple-echo acquisitions as compared to the single spin-echo experiments. The effects, while relatively small, are consistent across all areas. Additionally, the FA values in the isotropic medium (PBS) become smaller and closer to zero when calculated with a larger number of images, as predicted previously by Pierpaoli and Basser [3]. Their simulations have shown that FA values calculated with high S/N data should be extremely accurate for anisotropic media, but in the case of isotropic diffusion, FA approaches its true value of 0 very slowly even when a large number of very high S/N images are used. This is because FA cannot have a negative value, and thus any variation due to noise is reflected in a non-zero FA. These predictions are consistent with the data presented in Table 2.

The diffusion coefficient values are in close agreement with previously published data [21,22] and also the FA values calculated from these data [22]. It is worth noting that the error bars and quality of calculated maps are improved using 21 images from the multi-echo acquisition in comparison with the 13 images obtained using the standard acquisition. The results thus represent both improved quality and increased time efficiency since the 21 combined

Table 2
FA values for gray and white matter regions of the spinal cord and for water, collected from single-echo experiment (7 and 13 images) and multiple-echo experiment (21 and 39 images)

		FA from 2.2 h experiment, ±SD		FA from 4.1 h experiment, ±SD	
	Number of images used:	7 images (single-echo experiment)	21 images (multiple-echo experiment)	13 images (single-echo experiment)	39 images (multiple-echo experiment)
Water (control)		0.17 ± 0.07	0.11 ± 0.04	0.15 ± 0.05	0.09 ± 0.03
Dorsal columns white matter		0.84 ± 0.19	0.84 ± 0.15	0.83 ± 0.17	0.89 ± 0.15
Gray matter		0.33 ± 0.10	0.24 ± 0.08	0.30 ± 0.09	0.23 ± 0.07

The water data come from a separate experiment.

Table 3
Tr values for gray and white matter regions of the spinal cord and for water, collected from single-echo experiment (7 and 13 images) and multiple-echo experiment (21 and 39 images)

		Tr/3 from 2.2 h experiment ($\times 10^{-3}$ mm^2/s ± SD)		Tr/3 from 4.1 h experiment ($\times 10^{-3}$ mm^2/s ± SD)	
	Number of images used:	7 images (single-echo experiment)	21 images (multiple-echo experiment)	13 images (single-echo experiment)	39 images (multiple-echo experiment)
Water (control)		2.00 ± 0.20	1.97 ± 0.13	1.95 ± 0.15	2.00 ± 0.11
Dorsal columns white matter		0.39 ± 0.15	0.42 ± 0.08	0.41 ± 0.11	0.40 ± 0.07
Gray matter		0.36 ± 0.08	0.37 ± 0.04	0.37 ± 0.07	0.40 ± 0.03

The water data come from a separate experiment.

Table 4
FA values for ventral cord white matter, from experiments on three spinal cords

Experiment	1	2	3
Single-echo, 7 image experiment	0.74 ± 0.16	0.74 ± 0.15	0.74 ± 0.16
Single-echo, 13 image experiment	0.80 ± 0.14	0.75 ± 0.15	0.75 ± 0.15
Multiple-echo, 21 image experiment	0.84 ± 0.13	0.75 ± 0.09	0.76 ± 0.14
Multiple-echo, 39 image experiment	0.84 ± 0.11	0.79 ± 0.08	0.78 ± 0.12

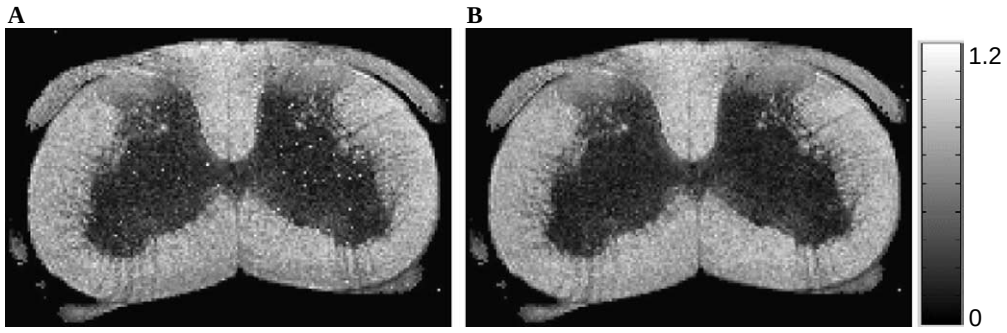

Fig. 3. High resolution (23 μm × 23 μm × 500 μm, voxel volume 0.32 nL) FA maps constructed from (A) 13 spin-echo images and (B) 39 images (13 spin-echo and 26 gradient-echo).

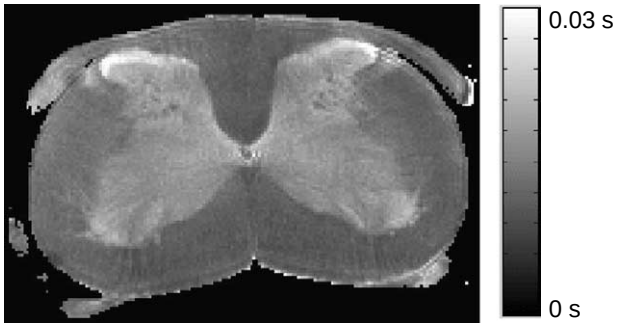

Fig. 4. T_2^* map (23 μm × 23 μm × 500 μm, voxel volume 0.32 nL).

gradient- and spin-echo images are obtained in close to half the data acquisition time of the 13 spin-echo image experiment. This method therefore offers significant advantages for ADT microimaging.

The efficiency of the multiple-echo method is also illustrated in Fig. 3, depicting FA maps for the higher resolution data set with an in-plane resolution of 23 μm and voxel volume of 0.32 nL. At this higher resolution, the quality-of-fit for the 39 image data set is superior to that from 13 images, resulting in the improved appearance of the FA map at no extra time cost. A quantitative comparison of the standard deviations of the measurements confirms the appearance; the FA in this experiment in the ventral columns measured with 13 diffusion weighted spin-echo images is 0.79 ± 0.13, while with 39 spin/gradient echo images it is 0.84 ± 0.09. Similarly for gray matter, the spin-echo experiment yields an FA of 0.27 ± 0.13 as compared to 0.23 ± 0.08 for the spin/gradient echo sequence. Finally, the T_2^* map obtained from the multiple-echo method is an added benefit of the multiple-echo acquisition and may also prove useful in tissue characterization by MRI microscopy, as recent work on myocardial architecture indicates [23].

As noted previously, multiple spin-echo manipulation has also been employed to reduce imaging time in ADT microimaging [5]. In our experience, the method presented here is more robust and easier to implement than the sequence in [5], and can be easily implemented on a system that is already equipped with a standard ADT spin-echo sequence. The multiple spin-echo method [5] requires precise calibration of the flip angles used in the sequence for accurate ADT determination. In addition to problems from spurious echoes and odd/even echo signal oscillations, for inhomogeneous B_1 fields that can be caused at high magnetic field strengths by samples with high dielectric constants, or for transmit-receive surface coil applications, the multiple spin-echo methods provide accurate measurements only from a very spatially limited region.

Clearly, this new sequence proposed here is more sensitive to B_0 inhomogeneities than are purely spin-echo based methods. The dependence of the gradient-echo intensity on the tissue T_2^* value means that the gain in efficiency is not as high as with multiple spin-echoes, particularly in cases where $T_2^* \ll T_2$. The length of the echo train acquired is determined both by S/N considerations and the need to provide sufficient diffusion weighting in each echo. In our case, we were consistently able to collect two additional gradient-echoes, but not a third one with significant additional diffusion weighting. For tissues or voxels with extremely short T_2^*, the acquisition of higher echoes might be of no additional benefit or could even potentially worsen the measurement uncertainties as compared to a single spin-echo. In such a case, an iterative fitting procedure could be employed where the first step is a voxelwise check performed to determine how

many echoes are above the noise level and can therefore be included in the fit. Unlike EPI, the sensitivity of this sequence to B_0 inhomogeneities does not contribute to significant image distortion. This is because distortion artifacts in EPI stem from the fact that each echo has a different phase encoding, leading to a rotation of the acquisition plane in k–t space versus the Cartesian grid [24].

A possible complication in the application of this method would be in the presence of restricted diffusion, i.e., where the mean free path of the protons is on the order of the length of time between diffusion pulses. This is because Δ is larger for the first echo than for the second and third echoes. Thus, the effective diffusion time is greater in the spin-echo than the later gradient-echoes, potentially introducing differential behavior with respect to restricted diffusion in the first echo, as the dephasing in the later echoes could be unaffected by this restriction. The potential for this problem cannot be completely eliminated, unless diffusion times are made equal for all echoes. However, in practice, this possibility can be minimized by judicious choice of diffusion times. For example, in the case of a healthy rat spinal cord, the diffusion coefficient perpendicular to the long axis of the cord in white matter is approximately 0.2×10^{-3} mm^2/s. After a diffusion time Δ of 6 ms as employed in our experiment for the first echo, the root mean squared (rms) unidirectional displacement in one dimension is 1.5 μm, smaller than the compartment size of 2–3 μm estimated using q-space imaging [25], suggesting that any differences with respect to restricted diffusion are negligible. Moreover, when the spin-echo diffusion time is chosen carefully, this method potentially can be used to partially alleviate restricted diffusion effects. As pointed out by LeBihan [26], trains of alternating bipolar gradient pulses can be used as an alternative to separating diffusion gradients by long Δ times, in order to minimize from the effects from restricted diffusion. This is effectively the situation encountered in our sequence, where additional diffusion weighting after the first echo is achieved using bipolar gradient pairs. Since the longest diffusion time encountered is the Δ during the first echo, the effective maximal rms displacement encountered with this sequence will be typically smaller for a given b-factor, as compared to a conventional spin-echo diffusion sequence where Δ is often purposefully extended in order to achieve extra diffusion weighting.

Future considerations for improvement to the work presented here include optimization of the diffusion weighting so that the directions of the b-vectors cover "b-space" evenly, and acquisition of multiple spin-echoes surrounded by gradient-echoes as employed, for example, with GRASE (gradient- and spin-echo) sequences [27], potentially allowing a significant further reduction in acquisition time. Also, combination of multiple-echo acquisition with reduced-encoding methods [15] may help to further improve imaging efficiency for microscopy.

Acknowledgments

We thank Andre Müller from the Neurology Department of the University Hospital in Regensburg, Germany, for providing us with the spinal cord samples. V.G., T.N., and A.W. gratefully acknowledge the financial support of the Alexander von Humboldt Stiftung, Wolfgang Paul Preis. The authors thank the reviewers for their help in improving the manuscript, and in particular, for their suggestion of the addition of Table 1 to simplify for the reader the various gradient configurations employed here.

References

[1] P.J. Basser, J. Mattiello, D. LeBihan, Estimation of the effective self-diffusion tensor from the NMR spin-echo, J. Magn. Reson. Ser. B 103 (1994) 247–254.
[2] P.J. Basser, J. Mattiello, D. LeBihan, MR diffusion tenser spectroscopy and imaging, Biophys. J. 66 (1994) 259–267.
[3] C. Pierpaoli, P.J. Basser, Toward a quantitative assessment of diffusion anisotropy, Magn. Reson. Med. 36 (1996) 893–906.
[4] E.W. Hsu, L.A. Setton, Diffusion tensor microscopy of the intervertebral disc anulus fibrosus, Magn. Reson. Med. 41 (1999) 992–999.
[5] V. Gulani, G.A. Iwamoto, H. Jiang, J.S. Shimony, A.G. Webb, P.C. Lauterbur, A multiple echo pulse sequence for diffusion tensor imaging and its application in excised rat spinal cords, Magn. Reson. Med. 38 (1997) 868–873.
[6] B.A. Inglis, L. Yang, E.D. Wirth, D. Plant, T.H. Mareci, Diffusion anisotropy in excised normal rat spinal cord measured by NMR microscopy, Magn. Reson. Imag. 15 (1997) 441–450.
[7] J. Zhang, P.C.M. van Zijl, S. Mori, Three-dimensional diffusion tensor magnetic resonance microimaging of adult mouse brain and hippocampus, NeuroImage 15 (2002) 892–901.
[8] J. Zhang, L.J. Richards, P. Yarowsky, H. Huang, P.C.M. van Zijl, S. Mori, Three-dimensional anatomical characterization of the developing mouse brain by diffusion tensor microimaging, NeuroImage 20 (2003) 1639–1648.
[9] E.W. Hsu, A.L. Muzikant, S.A. Matulevicius, R.C. Penland, C.S. Henriquez, Magnetic resonance myocardial fiber-orientation mapping with direct histological correlation, Am. J. Physiol. Heart Circ. Physiol. 274 (1998) H1627–H1634.
[10] Y. Jiang, K. Pandya, O. Smithies, E.W. Hsu, Three-dimensional diffusion tensor microscopy of fixed mouse hearts, Magn. Reson. Med. 52 (2004) 453–460.
[11] E.W. Hsu, S. Mori, Analytical expressions for the NMR apparent diffusion coefficients in an anisotropic system and a simplified method for determining fiber orientation, Magn. Reson. Med. 34 (1995) 194–200.
[12] T.E. Conturo, R.C. McKinstry, E. Akbudak, B.H. Robinson, Encoding of anisotropic diffusion with tetrahedral gradients: a general mathematical diffusion formalism and experimental results, Magn. Reson. Med. 35 (1996) 399–412.
[13] J. Hennig, Echoes—how to generate, recognize, use or avoid them in MR imaging sequences, part 2, Concepts Magn. Reson. 3 (1991) 179–192.
[14] J. Hennig, Echoes–how to generate, recognize, use or avoid them in MR imaging sequences, part 1, Concepts Magn. Reson. 3 (1991) 125–143.
[15] E.W. Hsu, C.S. Henriquez, Myocardial fiber orientation mapping using reduced encoding diffusion tensor imaging, J. Cardiovasc. Magn. Reson. 3 (2001) 339–347.
[16] L. Li, C.H. Sotak, Diffusion measurements by pulsed field-gradient multiple spin echoes, J. Magn. Reson. 92 (1991) 411–420.
[17] A.P. Crawley, R.M. Henkelman, Errors in T2 estimation using multislice multiple-echo imaging, Magn. Reson. Med. 4 (1987) 34–47.

[18] M.H. Levitt, R. Freeman, NMR population-inversion using a composite pulse, J. Magn. Reson. 33 (1979) 473–476.
[19] C.F. Beaulieu, X. Zhou, G.P. Cofer, G.A. Johnson, Diffusion-weighted MR microscopy with fast spin-echo, Magn. Reson. Med. 30 (1993) 201–206.
[20] S. Mori, P.C. van Zijl, A motion correction scheme by twin-echo navigation for diffusion-weighted magnetic resonance imaging with multiple RF echo acquisition, Magn. Reson. Med. 40 (1998) 511–516.
[21] J.C. Ford, D.B. Hackney, D.C. Alsop, H. Jara, P.M. Joseph, C.M. Hand, P. Black, MRI characterization of diffusion-coefficients in a rat spinal-cord injury model, Magn. Reson. Med. 31 (1994) 488–494.
[22] V. Gulani, A.G. Webb, I.D. Duncan, P.C. Lauterbur, Apparent diffusion tensor measurements in myelin-deficient rat spinal cords, Magn. Reson. Med. 45 (2001) 191–195.
[23] S. Kohler, K.H. Hiller, C. Waller, W.R. Bauer, A. Haase, P.M. Jakob, Investigation of the microstructure of the isolated rat heart: a comparison between T_2^*—and diffusion-weighted MRI, Magn. Reson. Med. 50 (2003) 1144–1150.
[24] F. Hennel, Multiple-shot echo-planar imaging, Concepts Magn. Reson. 9 (1997) 43–58.
[25] Y. Assaf, A. Mayk, Y. Cohen, Displacement imaging of spinal cord using q-space diffusion-weighted MRI, Magn. Reson. Med. 44 (2000) 713–722.
[26] D. LeBihan, Diffusion and Perfusion Magnetic Resonance Imaging, Raven Press, New York, 1995.
[27] K. Oshio, D.A. Feinberg, GRASE (Gradient- and spin-echo) imaging: a novel fast MRI technique, Magn. Reson. Med. 20 (1991) 344–349.